Soft-X-Ray Spectroscopy Study of Nanoscale Materials

Jinghua Guo
Advanced Light Source, Lawrence Berkeley National Laboratory, Berkeley, CA 94720, USA

ABSTRACT

The ability to control the particle size and morphology of nanoparticles is of crucial importance nowadays both from a fundamental and industrial point of view considering the tremendous amount of high-tech applications. Controlling the crystallographic structure and the arrangement of atoms along the surface of nanostructured material will determine most of its physical properties. In general, electronic structure ultimately determines the properties of matter. Soft X-ray spectroscopy has some basic features that are important to consider. X-ray is originating from an electronic transition between a localized core state and a valence state. As a core state is involved, elemental selectivity is obtained because the core levels of different elements are well separated in energy, meaning that the involvement of the inner level makes this probe localized to one specific atomic site around which the electronic structure is reflected as a partial density-of-states contribution. The participation of valence electrons gives the method chemical state sensitivity and further, the dipole nature of the transitions gives particular symmetry information. The new generation synchrotron radiation sources producing intensive tunable monochromatized soft X-ray beams have opened up new possibilities for soft X-ray spectroscopy. The introduction of selectively excited soft X-ray emission has opened a new field of study by disclosing many new possibilities of soft X-ray resonant inelastic scattering. In this paper, some recent findings regarding soft X-ray absorption and emission studies of various nanostructured systems are presented.

Keywords: Soft X-ray absorption and emission spectroscopy, synchrotron radiation, nanostructured materials

1. INTRODUCTION

The ability to control the particle size and morphology of nanoparticles is of crucial importance nowadays both from a fundamental and industrial point of view considering the tremendous amount of high-tech applications of nanostructured metal oxide materials devices such as dye-sensitized solar cells, displays and smart windows, chemical, gas and biosensors, lithium batteries, supercapacitors. Controlling the crystallographic structure and the arrangement of atoms along the surface of nanostructured material will determine most of its physical properties. In general, electronic structure ultimately determines the properties of matter, and it is therefore natural to anticipate that a complete understanding of the electronic structure of nanoscale systems will lead to a progress in nanoscience, not inferior to the one we have seen in recent years.

Soft X-ray spectroscopy has some basic features that are important to consider [1-4]. As a core state is involved, elemental selectivity is obtained because the core levels of different elements are well separated in energy, meaning that the involvement of the inner level makes this probe localized to one specific atomic site around which the electronic structure is reflected as a partial density-of-states contribution. The participation of valence electrons gives the method chemical state sensitivity and further, the dipole nature of the transitions gives particular symmetry information.

2. SOFT X-RAY SPECTROSCOPY

Synchrotron radiation has become an indispensible tool in many areas of science. Synchrotron radiation is the light emitted by electrons as they circulate around a high-energy accelerator. The use of synchrotron radiation has grown to a powerful research tool in science in the last decade. Vacuum ultraviolet and x-ray photons emerging from storage rings are today among the most frequently used probes for advanced investigation of the electronic and geometric structure of matter.

Current development in synchrotron radiation techniques has led to extremely bright undulator sources. The use of synchrotron radiation for the excitation of soft X-ray emission spectra adds several important qualities to this spectroscopic method. Firstly, it provides a very intense photon-excitation source; secondly, monochromatized soft X-ray photons offer higher degree of energy selectivity than do electrons. Thirdly, synchrotron radiation offers the possibility of exciting soft X-ray spectroscopy by polarized light.

The soft X-ray region ranges from about 50 eV to 1200 eV. Much of the biological and environmental science can be based on soft X-ray spectroscopy measurements. This is because the X-ray edges in this region offer routes to chemical information not readily obtained by other techniques. The edges in the soft X-ray region include: the light element *K*-edges, including C, N, O, F; the first transition metal *L*-edges including Ti, Cr, Mn, Fe, Co, Ni, Cu, Zn; the *M*-edges of Fe through to the lanthanides, and *N*-edges of the lanthanides etc. All the absorption edges can be found on a website of the Center for X-ray Optics, Lawrence Berkeley National Laboratory [5].

2.1 X-RAY ABSORPTION AND EMISSION SPECTROSCOPY

Soft X-ray absorption spectrum provides information about the unoccupied states. For example, in carbon *K*-edge absorption, the carbon *1s* electron is excited to empty electronic states in the carbon allotrope conduction band, and the dipole selection rule provides a tool to study locally the C *2p* character of these unoccupied valence band (Fig.1) The atomic nature of the core hole implies elemental and site selectivity. The probability of such a transition is related to the X-ray absorption cross section. The intensity of these secondary electrons or the photons can be measured as a function of incoming photon energy. This will reflect the absorption cross section as the intensity of the secondary electrons/emitted photons are proportional to the absorbed intensity. Because of the short mean free path of electrons, the electron-yield-detection method is very surface sensitive. If the out coming photons are detected (fluorescence yield), the X-ray absorption becomes bulk probing (about 100-200 nm) due to the comparatively larger attenuation lengths.

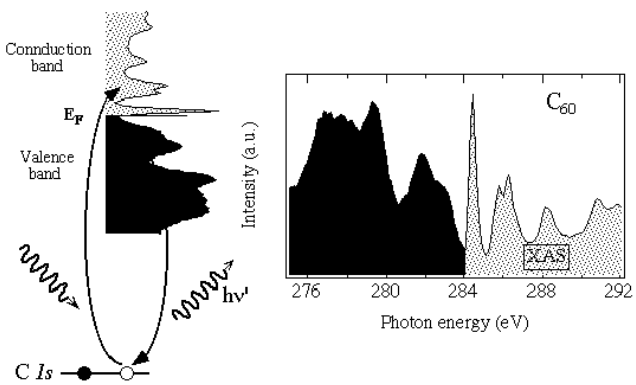

Figure 1. Schematic representation x-ray absorption and emission processes.

In soft X-ray emission, the core vacancy left by the excited *1s* electron is filled by a valence-orbital electron, thereby also giving direct information about the chemical bonding. The interest in the technique is presently booming due to the advent of third generation synchrotron radiation sources. In addition to the inherent elemental selectivity of X-ray spectra, energy selective excitation allows separation of features that pertain to different atoms of a sample. Emission from chemically non-equivalent sites of the same atomic species can be separated.

2.2 RESONANT SOFT X-RAY EMISSION SPECTROSCOPY

The big improvement in the performance of synchrotron radiation based soft-X-ray spectroscopy from last decade is the high brightness of the third generation source combined with high quality optical systems for refocusing the monochromatized soft-X-ray beam. The new generation synchrotron radiation sources, producing intense tunable

monochromatized X-ray beams, have opened up new possibilities for soft X-ray spectroscopy. X-ray absorption and emission have been traditionally treated as two independent processes, with the absorption and emission spectra providing information on the unoccupied and occupied electronic states, respectively.

The possibility to select the energy of the excitation has created an extra degree of freedom compared to the traditional spectroscopy pursued with high-energy electron or characteristic X-ray excitation. The energy selectivity makes it possible to perform resonant excitation, i.e. exciting to particular empty states [6-8]. The introduction of selectively excited soft X-ray emission has opened a new field of study by disclosing many new possibilities of soft X-ray resonant inelastic scattering (RIXS). Among the new tools available with this technique one can mention site selectivity in high-T_c superconducting materials [9], ultrafast dynamics [10] and chemical bonding mechanism [11] by detuning from resonance, etc.

For *L*-edge and *M*-edge RIXS, the final states are typical *d-d* excitations [12-13]. Final states probed via such a channel, RIXS or XRS, are related to eigenvalues of the ground state Hamiltonian. The core-hole lifetime is not a limit on the resolution in this spectroscopy. According to the many-body picture, the energy of a photon scattered on a certain low-energy excitation, should change by the same amount as a change in the excitation energy of the incident beam, so that inelastic scattering structures have constant energy losses and follow the elastic peak on the emitted-photon energy scale. Further discussion on resonant soft X-ray emission spectroscopy can be found in the earlier reviews [14-17].

2.3 EXPERIMENTAL DETAILS

An outline of an undulator beamline, such as beamline 7.0.1 of the Advanced Light Source [18], is presented in Fig.2, showing its principle elements. It comprises of an undulator of 5 meter and 5-cm-period and a spherical grating monochromator (SGM) covering the spectral range from 60 to 1200 eV. It is designed for high-resolution operation with maximum photon flux and a small spot size (typically, 50 - 100 mm) at the sample, matched to the acceptance of the experiment spectrometers.

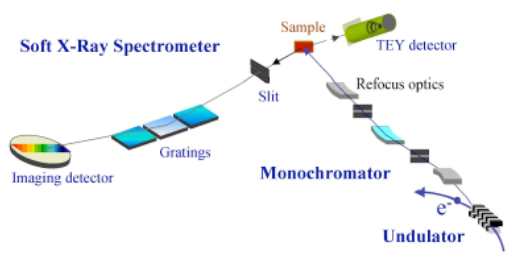

Figure 2. An outline of an undulator beamline including an undulator, monochromator and a Rowland circle geometry grating spectrometer and channeltron for soft-x-ray fluorescence detection.

The experimental set-up at a synchrotron radiation beamline is called the end-station, since it constitutes an interchangable experiment at the end of the beamline. The end-station is comprised of three main parts: analysis chamber, preparation chamber and loadlock chamber, separated by valves [19].

X-ray absorption spectra are recorded in total-electron-yield (TEY) mode or fluorescence-yield (FY) mode. Total electron yield is measured from sample drain current, and the fluorescence yield is obtained from channeltron. X-ray emission spectra are recorded by using a grazing incidence grating spectrometer.

The high resolution grating spectrometer was mounted parallel to the polarization vector of the incident photon beam to detect the emitted X-ray. The grazing-incidence grating spectrometer is based on Rowland geometry. It consists of slit, gratings and detector. Three spherical gratings are optimized to cover an operation range of 50-1000 eV. The gratings are mounted at angles of incidence to have a joint fixed slit, and the emitted X-rays are detected using a two-dimensional detector that can be positioned and oriented tangentially to the pertained Rowland circle. The detector consists of multi channel plates and a resistive anode with a four-electrode readout.

3. CHEMICAL SENSITIVITY OF SOFT X-RAY SPECTROSCOPY

The advantages of soft X-ray spectroscopy have stemmed from the electric-dipole nature of the electronic transitions. The emission is originating from an electronic transition between a localized core state and a valence state. The energy of the emitted X-ray is equal to the difference in energy of the two states. The involvement of the inner level makes this probe localized to one specific atomic site around which the electronic structure is reflected as a partial density-of-states (DOS) contribution. Chemical sensitivity is obtained when the resolution of the detected emission lines is high enough to resolve fine structure. The line shapes are determined by the valence electron distribution and the transitions are governed by dipole selection rules. For solids essentially a partial DOS mapping is obtained.

In the nano-regime, two effects dominate the chemical and physical properties: (i) increasing contribution of surface atoms (surface effect). Surface atom to bulk atom ratio increases dramatically as the particles size decreases. For a 30-nm particle, about 5% of all the atoms are on the surface, while for 3 nm particle, up to 50% of all the atoms are on the surface, (i) quantum confinement as the nanoclusters down to a few nanometers (size effect), where electrons will then begin to feel the effects of quantum confinement when the size of the structure becomes comparable to the electron wavelengths.

Synchrotron radiation with photon energy at or below 1 keV is giving new insight into such areas as wet cell biology, condensed matter physics and extreme ultraviolet optics technology. In the soft x-ray region, the question tends to be, what are the electrons doing as they migrated between the atoms? [20,21].

3.1 ELECTRONIC STRUCTURE AND GEOMETRICAL STRUCTURE

The difference in the structural arrangement of carbon forms, such as graphite, diamond, C_{60}, and carbon nanotubes, gives rise to the wide differences in their physical properties. Carbon has an atomic number of 6 and has a $1s^2 2s^2 2p^2$ configuration in the electronic ground state. The atoms in diamond structure are bonded to their four nearest-neighbors using linear combinations of $2s$, $2p_x$, $2p_y$, and $2p_z$ orbitals in the sp^3 configuration. In contrast, in the graphite structure, strong in-plane bonds are formed between a carbon atom and its three nearest-neighbors from $2s$, $2p_x$, and $2p_y$ orbitals; this bonding arrangement is denoted by sp^2. The remaining electron with a p_z orbital provides only weak interplanar bonding, but it is responsible for the semi-metallic electronic behavior in graphite.

Fig. 3 displays X-ray absorption spectra of highly oriented pyrolytic graphite (HOPG) recorded at different incidence angles[21]. When the polarization vector of the incident beam is parallel to the basal plane only excitations to σ states are possible. Excitations to π states become more likely the more perpendicular to the basal plane the polarization vector is. Thus, one can see that the main feature below 292 eV has mainly π character, while the σ states are observed at energies above 292 eV. It should be noted that the sharp absorption feature appearing at 292.0 eV is not due to the band structure but to an excitonic state that was discussed in detail elsewhere [22-25].

The normal carbon K_α XES spectra of diamond, graphitic carbon, C_{70}, C_{60}, and benzene are presented in Fig. 4a, where large differences in spectral profile are observed. The spectra of diamond and graphitic carbon show the shape of a wide band with some shoulder structures where the energy positions of the peak maximum and band shapes are largely

different. In some studies related to vapor deposition the XES spectral profile has been used as a means to identify certain chemical states [14]. In contrast, the spectra of benzene, C_{60}, and C_{70} exhibit clearly resolved emission peaks indicating the strong molecular character in their solid phase. The marked resolved emission features in benzene can find their counterpart in the emission spectra of C_{60} and C_{70}, and all the fine structures are washed out in diamond and graphite.

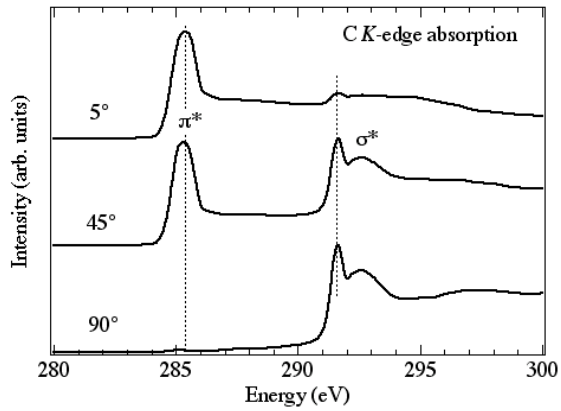

Figure 3. Polarization dependent X-ray absorption spectra of HOPG.

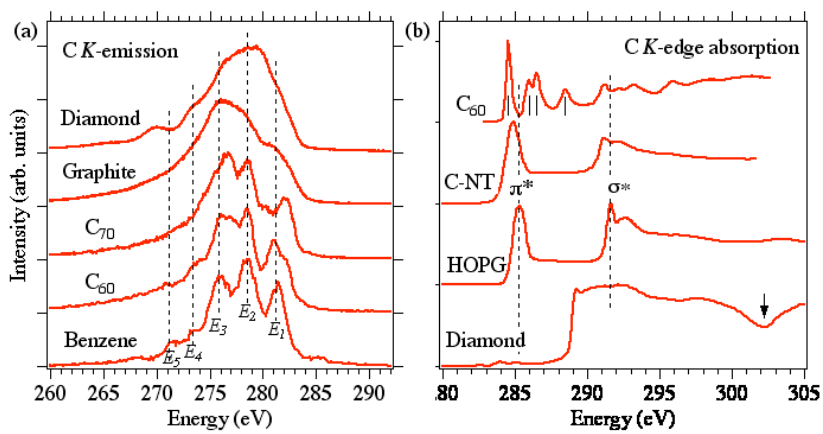

Figure 4. Non-resonant carbon K_a SXES spectra of diamond, amorphous carbon (graphitic), C_{70}, C_{60}, and benzene; (b) X-ray absorption spectra of C_{60}, carbon nanotubes, HOPG, and diamond.

Fig. 4b shows the x-ray absorption spectra of C_{60}, carbon nanotubes (C-NT), HOPG, and diamond. The X-ray absorption spectral shape of carbon nanotubes is similar to that of HOPG that is different to the one from C_{60}. The π* shows a shift towards low photon energy in the X-ray absorption of C-NT. C_{60} gives more resolved absorption features that indicate a strong molecular character of C_{60} with highly degenerated molecular orbitals due to its high symmetry. Non-resonant carbon K_α XES spectra of carbon nanotubes and C_{60} show a similar shape, but resonantly excited XES spectra reveal the large differences in the electronic structure of these two systems. XAS spectrum of diamond shows no π* contribution around 285 eV, and the absorption feature at 288.85 eV is assigned to the diamond exciton and followed with the σ* conduction band. The 2nd bandgap at 302 eV, as a fingerprint of the diamond structure, is also clearly observed.

3.2 Cu NANOCLUSTERS

Copper nanoclusters have been studied due to its potential applications in optics, magneto-electronics and catalyst systems [26-28]. Silicon carbide provides a structurally and chemically stable support for such nanoclusters due to its stability against copper [29]. Although there are some studies on copper island formation on silicon carbide, the reports relied on the indirect spectroscopic results mainly focusing in the stability of Cu/SiC interfaces [30-32]. Recently we have observed the morphology of the copper nanoclusters by high-resolution transmission electron microscopy (TEM) where copper nanoclusters had ellipsoid shape inside SiC matrix [33]. XAS studies can give a detailed description of the size dependence of the electronic structure of the copper nanoclusters to understand the nature of chemical bonds due to size effect.

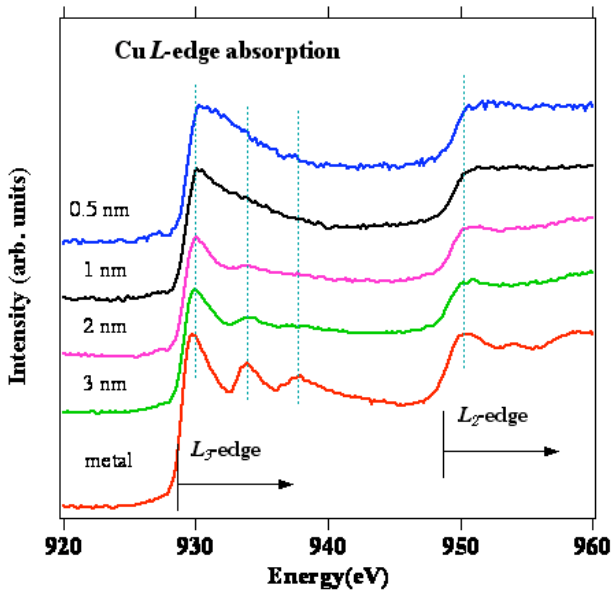

Figure 5. XAS spectra of Cu *L*-edge with different nanocluster sizes.

Fig. 5 shows the Cu *L*-edge XAS spectra of a series of Si/Ta(100nm)/[Cu(0.5nm-3nm)/SiC(2nm)]10/Ta(5nm) and the reference Cu. Bulk Cu sample shows three distinct features in the L_3-edge region, which are associated with the unoccupied *3d* states in Cu. In a free Cu atom, the *3d* orbital is fully occupied. In contrast, a solid Cu is characterized by a re-mixing of the valence wave functions in the ground state, gaining a small amount of non-vanishing *3d* hole. According to dipole-selection rules, the dominant transition in XAS of Cu is from the Cu $2p_{3/2}$ and $2p_{1/2}$ states to the unoccupied Cu *3d* states [34]. Thus, the peak at the onset of L_3-edge is associated with the Cu *3d* -derived character due to the *3d-4s* hybridization, which gives a sharp $2p \rightarrow 3d$ transition superimposed on the smooth $2p \rightarrow 4s$ transitions. The peak at 939 eV and the peak at 943 eV are attributed to transitions towards empty states, mainly mixed with *s*, *p* characters. As the nanocluster size decreases, two distinct changes occur. First, the peaks move slightly to the higher energy. Second, the peaks at 939 eV and 943 eV drastically decrease in intensity. The decrease of these peaks indicates that the *s-p-d* hybridization becomes weaker. This behavior can be attributed to the surface effect. The Cu atoms at surface have lower coordination number and see less Cu neighbor atoms around, giving rise to a reduction of Cu-Cu interaction. For Cu-Cu interaction is mainly determined by *d-d* interaction and stronger Cu *d-d* interaction favors *s-p-d* re-hybridization, the reduction of *d* electron will weaken the hybridization.

3.2 ZnO NANOCRYSTAL

ZnO, a wide band-gap semiconductor, has attracted a considerable attention during the last years due to its potential technological applications such as, for instance, high efficient vacuum fluorescent displays (VFD) and field-emission displays [35]. ZnO has also been used for short wavelength laser devices [36], high power and high frequency electronic devices [37], and light-emitting diodes (LED) [38-39]. ZnO shows many advantages: (i) it has a larger exciton energy (60

meV) than GaN (23 meV); (ii) the band-gap is tunable from 2.8 to 4 eV [40,41]; (iii) wet chemical synthesis is possible; (iv) low power threshold at room temperature; (v) dilute Mn doped ZnO shows room temperature ferromagnetism [42]. Recently, quantum size effects on the exciton and band-gap energies were observed in semiconductor nanocrystals [43,44]. The controlled synthesis of ZnO nanostructures and in-depth understanding of their chemical/physical properties and electronic structure are the key issues for the future development of ZnO based nanodevices.

The XES spectra of bulk and nanotructured ZnO are displayed together with the corresponding XAS spectrum in Fig. 6 [45]. The O *K*-edge emission spectrum reflects the O *2p* occupied states (valence band), and the O *K*-edge absorption spectrum reflects the O *2p* unoccupied states (conduction band). In the photon energy region of 530-539 eV, the X-ray absorption can be mainly assigned to the O *2p* hybridized with Zn *4s* states. In the region of 539-550 eV the spectrum is mainly attributed to O *2p* hybridized with Zn *4p* states. Above 550 eV, the contribution is mainly coming from O *2p* - Zn *4d* mixed states [46]. Stronger *s-p-d* hybridization was revealed in nanostructured ZnO since the contributions of features at 520 eV and 523 eV are enhanced. A well-defined band-gap can be observed between the valence-band maximum and conduction-band minimum. Our absorption-emission spectrum yields the fundamental band-gap energy of 3.3 eV.

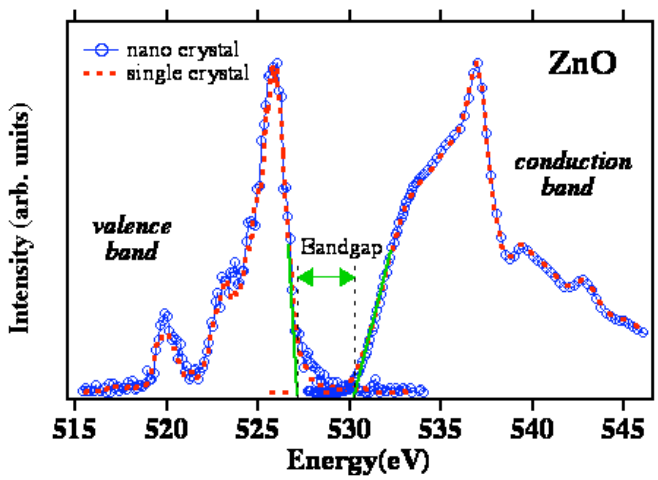

Figure 6. Oxygen X-ray absorption-emission spectrum reflected conduction band and valence band near the Fermi-level of ZnO nanoparticles in comparison with bulk ZnO.

3.3 Li INTERCALATED NANO POROUS TiO_2

Lithium insertion of nanoporous anatase TiO_2 electrodes for use in electrochemical processes has been studied using resonant inelastic soft-x-ray scattering spectroscopy [47]. The interest in nanostructured TiO_2 is based on the possibilities of using the material in various applications as batteries [48], displays [49] and dye sensitized solar cells. The electrode consists of interconnected nanocrystallites forming a nanoporous structure with an extremely large inner surface allowing for electrochemical reactions to take place in almost the entire volume of the electrode. High charging capacities are reported, when lithium is inserted into the nanoporous anatase titanium dioxide electrode. For technical devices, the reversibility of the reaction is of prime importance.

Fig. 7 shows Ti $L_{2,3}$ absorption and emission spectra recorded after insertion of lithium ions (x = 0.2) into the titanium dioxide electrode. Inspection of the absorption spectra shows that the features *a* and *b* are reduced in intensity compared with pure TiO_2 and the intensity of the L_3 e_g feature is redistributed towards lower energy. This is interpreted as due to Ti^{3+} contributions. In the doped case we can describe the spectral shape as a linear combination of Ti^{4+} and Ti^{3+} contributions (TiO_2 and $LiTiO_2$). The Ti^{3+} contribution is mapped out by scanning the photon energy over the Ti *2p* absorption edge while recording the Ti *3d* band-gap photoemission peak. As the photon energy is scanned, the band-gap peak resonates. This peak is integrated and plotted as a function of photon energy with L_3 and L_2 parts but shifted towards lower energy. The Ti $2p_{3/2}$ core level shift between Ti^{4+} and Ti^{3+} peaks in Li_xTiO_2 is 2.1 eV [50].

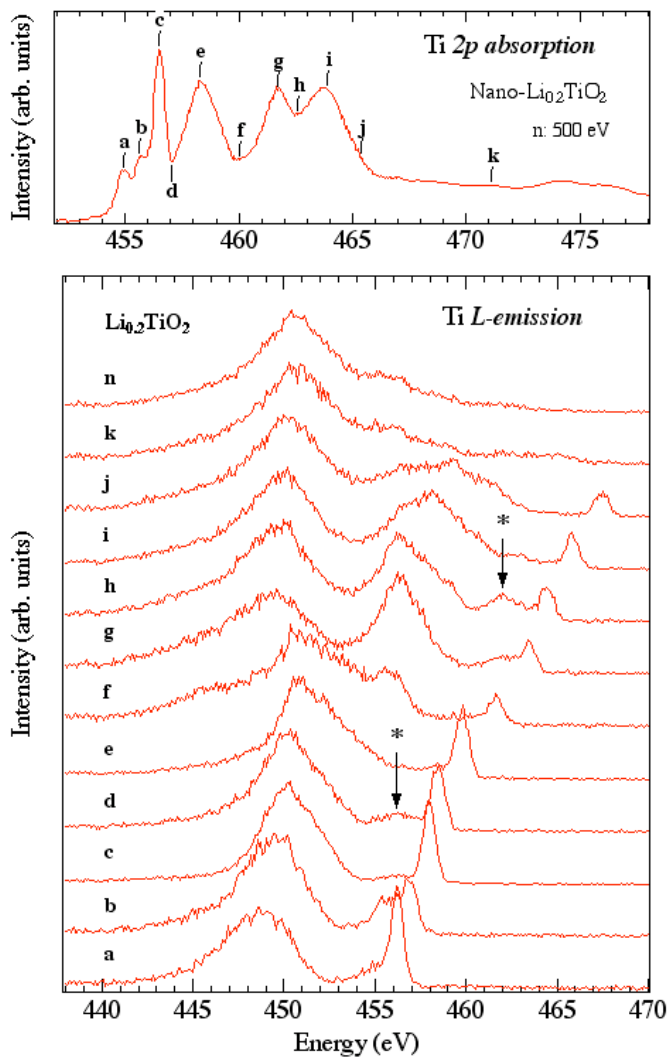

Figure 7. Ti *2p* absorption spectrum and resonantly excited *L*-emission of $Li_{0.2}TiO_2$ nano-materials.

A smaller shift is observed in the absorption spectra that could be due to screening effects. The two parts in the Ti^{3+} spectrum are split into t_{2g} and e_g by the crystal field. The delineation of the Ti^{3+} contribution to the XAS spectrum facilitates the understanding of the inelastic contributions in the resonant x-ray emission spectrum shown below the absorption panel in Fig. 7. The emission spectra significantly differ from the spectra of the undoped sample. Several low energy-loss features show up in the band gap of TiO_2, extending several eV below the elastic peak, which are not present in the undoped material. These energy-loss features are assigned to *d-d* excitations. They correspond to electron-hole pairs within or between the valence and conduction bands. This is a result of lithium insertion, which leads to an electron in the *d*-band (d^1) i.e. t_{2g}-states are occupied. In spectrum a, an asymmetric lineshape of elastic peak is observed and at the next excitation energy (b) this develops into a shoulder/peak. These low-energy excitations at 1.1 eV are attribute to electron-hole pairs within the t_{2g} band. The intensity of these excitations is enhanced when the excitation energy is tuned to the Ti^{3+} - t_{2g} absorption feature i.e. the final state in the scattering process is an excited electron in the t_{2g} band. The relative intensity of the inelastic part is quite large. This is an indication of significant electron correlation in the system.

ACKNOWLEDGEMENTS

I would like to acknowledge the contributions from my collaborators: A. Augustsson, Chungli Dong, L. Vayssieres, S. Mao, D. W. Shin, M. Mattesini, C. Persson, Y. Luo, J. Nordgren, etc. The Advanced Light Source is supported by the Director, Office of Science, Office of Basic Energy Sciences, of the U.S. Department of Energy under Contract No. DE-AC02-05CH11231.

REFERENCES

1. Tsun-Kong Sham, ed. *Chemical Applications of Synchrotron Radiation* (World Scientific, Singapore, 2002). Chapter 10 "Soft x-ray fluorescence spectroscopy for materials science and chemical physics", J. Nordgren, S.M. Butorin, L.C. Duda, J.-H. Guo, J.E. Rubensson, p. 517.

2. J. A. Samson and D. L. Ederer, ed. *Vacuum Ultraviolet Spectroscopy*. (Academic Press, London, 2000). Chapter 13, "Soft x-ray fluorescence spectroscopy", T. A. Callcott, p.279

3. Frank de Groot, Chem. Rev. **101**, 1779 (2001).

4. Joachim Stohr, *NEXAFS Spectroscopy*. (Springer-Verlag, Berlin Heidelberg, 1992).

5. *http://www.cxro.lbl.gov/optical_constants/*

6. J. Nordgren and N. Wassdahl, J. Electr. Spectr. and Related Phenom. **72**, 273 (1995).

7. J. Nordgren, J. Electr. Spectr. and Related Phenom. **78**, 25 (1996).

8. J. Nordgren, P. Glans, K. Gunnelin, J.-H. Guo, P. Skytt, C. Såthe, N. Wassdahl, Appl. Phys. A **65**, 97 (1997).

9. J.-H. Guo, S. M. Butorin, N. Wassdahl, P. Skytt, J. Nordgren, and Y. Ma, Phys. Rev. B **49**, 1376 (1994).

10. P. Skytt, P. Glans, J.-H. Guo, K. Gunnelin, C. Såthe, J. Nordgren, F. Kh. Gel'mukhanov, A. Cesar, and H. Ågren, Phys. Rev. Lett. **77**, 5035 (1996).

11. Mats Nyberg, Yi Luo, L. Qian, J.-E. Rubensson, C. Såthe, D. Ding, J.-H. Guo, T. Kaambre, and J. Nordgren, Phys. Rev. B **63**, 115117 (2001).

12. S. M. Butorin, J.-H. Guo, M. Magnuson, P. Kuiper, and J. Nordgren, Phys. Rev. B **54**, 4405 (1996).

13. P. Kuiper, J.-H. Guo, C. Såthe, L.-C. Duda, J. Nordgren, J. J. M. Pothuizen, F. M. F. de Groot, and G. A. Sawatzky, Phys. Rev. Lett.**80**, 5204 (1998).

14. J.-H. Guo and J. Nordgren, J. Electron Spectrosc. Relat. Phenom. J. Electron Spectrosc. Relat. Phenom. **110-111**, 105 (2000).

15. S. M. Butorin, J. Electron Spectrosc. Relat. Phenom. **110-111**, 213 (2000).

16. S. M. Butorin, J.-H. Guo, N. Wassdahl, and J. E. Nordgren, J. Electron Spectrosc. Relat. Phenom. **110-111**, 235 (2000).

17. A. Kotani and S. Shin, Rev. Mod. Phys. **73**, 203 (2001).

18. T. Warwick, P. Heimann, D. Mossessian, W. McKinney and H. Padmore,Rev. Sci. Instrum. **66**, 2037 (1995).

19. J.-H. Guo, N. Wassdahl, P. Skytt, S. M. Butorin, L.-C. Duda, C. J. Englund, and J . Nordgren, Rev. Sci. Instrum. **66**, 1561 (1995).

20. N. Smith, Physics Today, January 29 (2001).

21. Jinghua Guo, Int. J. Nanotechnology, **1-2**, 193-225 (2004).

22. P. Skytt, P. Glans, D. C. Mancini, J.-H. Guo, N. Wassdahl, J. Nordgren, and Y. Ma, Phys. Rev. B **50**, 10457 (1994).

23. Y. Ma, N. Wassdahl, P. Skytt, J.-H. Guo, J. Nordgren, P. D. Johnson, J.-E. Rubensson, T. Boske, W. Eberhardt, and S. D. Kevan, Phys. Rev. Lett. **69**, 2598 (1992).

24. Y. Ma, P. Skytt, N. Wassdahl, P. Glans, D. C. Mancini, J.-H. Guo, and J. Nordgren, Phys. Rev. Lett. **71**, 3725 (1993).

25. J. A. Carlisle, E. L. Shirley, E. A. Hudson, L. J. Terminello, T. A. Calcott, J. J. Jia, D. L. Ederer, R. C. C. Perera, and F. J. Himpsel, Phys. Rev. Lett. **74**, 1234 (1995).

26. R. L. Zimmerman, D. Ila, E. K. Williams, B. Gasic, A. Elsamadicy, A. L. Evelyn, D. B. Poker, D. K. Hensley and David J. Larkin, Nucl. Instr. and Meth. B **166/167**, 892 (2000).

27. H. Fukuzawa, H. Yuasa, S. Hashimoto, K. Koi, H. Iwasaki, M. Takagishi, Y. Tanaka, M. Sahashi, IEEE, Trans. Magn, **40**, 2236 (2004).

28. Poul L. Hansen, Jakob B. Wagner, Stig Helveg, Jens R. Rostrup-Nielsen, Bjerne S. Clausen, and Henrik Topsøe, Science, **295**, 2053 (2002).

29. Katsumi Nishimori, Heizo Tokutaka, Shuuichi Nakanishi, Satoru Kishida and Naganori Ishihara, Jpn. J. Appl. Phys. Lett. **28**, L1345 (1989).

30. Z. An, A. Ohi, M. Hirai, M. Kusaka, M. Iwami, Surf. Sci. **493**, 182 (2001).

31. Z. An, M. Hirai, M. Kusaka, T. Saitoh, M. Iwami, Jpn. J. Appl. Phys. **40**, 1927 (2001).

32. I. Dontas, S. Ladas, S. Kennou, Diamond Relat. Mat. **12**, 1209 (2003).

33. D. W. Shin, S. X. Wang, A. Marshall, W. Kimura, C.L. Dong, A. Augustsson, J.-H. Guo, Thin Solid Films, **473**, 267 (2005).

34. H. H. Hsieh, Y. K. Chang, W. F. Pong, J. Y. Pieh, P. K. Tseng, T. K. Sham, I. Coulthard, S. J. Naftel, J. F. Lee, S. C. Chung, K. L. Tsang, Phys. Rev. B, **57**, 15204 (1998).

35. S. Shionoya and W. M Yen, eds. *Phosphor Handbook*, CRC Press, Boca Raton, FL, 1999, p.255.

36. J. Nause, S. Ganesan, B. Nemeth, V. Munne, A. Valencia, P. Keisel, H. Morkoc, D. Look, III-Vs Review **12**, 28 (1999).

37. M. W. Shin and R. J. Trew, Electronics Letter **31**, 498 (1995).

38. F. Hamdani, A. E. Botchkarev. H. Tang, W. Kim, and H. Morkoc, Appl. Phys. Lett. **71**, 3111 (1997).

39. T. Detchprohm, K. Hiramatsu, H. Amano, and I. Akasaki, Appl. Phys. Lett. **61**, 2688 (1992).

40. R. D. Vispute, V. Talyansky, S. Choopun, R. P. Sharma, T. Venkatesan, M. He, X. Tang, J. B. Halpern, M. G. Spencer, Y. X. Li, L. G. Salamanca-Riba, A. A. Iliadis, and K. A. Jones, Appl. Phys. Lett. **73**, 348 (1998)

41. A. Ohtomo M. Kawasaki, T. Koida, H. Koinuma, Y. Sakurai, Y. Yoshida, M. Sumiya, S. Fuke, T. Yasuda, Y. Segawa, Mater. Sci. Forum. **264**, 1463 (1998).

42. Parmanand Sharma, Amita Gupta, K.V. Rao, Frank J. Owens, Renu Sharma, Rajeev Ahuja, J. M. Osorio Guillen, Borje Johansson and G. A. Gehring, Nature Mater. **2**, 673 (2003).

43. T. van Buuren, L. N. Dinh, L. L. Chase, W. J. Siekhaus, and L. J. Terminello, Phys. Rev. Lett. **80**, 3803 (1998).

44. Y. K. Chang, H. H. Hsieh, W. F. Pong, M.-H. Tsai, F. Z. Chien, P. K. Tseng, L. C. Chen, T. Y. Wang, K. H. Chen, D. M. Bhusari, J. R. Yang, and S. T. Lin, Phys. Rev. Lett. **82**, 5377 (1999).

45. C. L. Dong, C. Persson, L. Vayssieres, A. Augustsson, T. Schmitt, M. Mattesini, R. Ahuja, C. L. Chang, and J.-H. Guo, Phys. Rev. B **70**, 195325 (2004).

46. J.-H. Guo, L. Vayssieres, C. Persson, R. Ahuja, B. Johansson, and J. Nordgren, J. Phys: Condens. Matter. **14**, 6969 (2002).

47. A. Augustsson, A. Henningsson, S. M. Butorin, H. Siegbahn, J. Nordgren, and J.-H. Guo, J. Chem. Phys. **119**, 3983 (2003).

48. S. Y. Huang, L. Kavan, I. Exnar, and M. Gratzel, J. Electrochem. Soc. **142**, L142 (1995).

49. A. Hagfeldt, N. Vlachopoulos, and M. Gratzel, J. Electrochem. Soc. **141**, L82 (1994).

50. S. Sodergren, H. Rensmo, and H. Siegbahn, ECASIA 97/7 John Wiley and Sons Ltd Chichester (3) (1997).

*jguo@lbl.gov; phone 1 510 495-2230; fax 1 510 495-2067